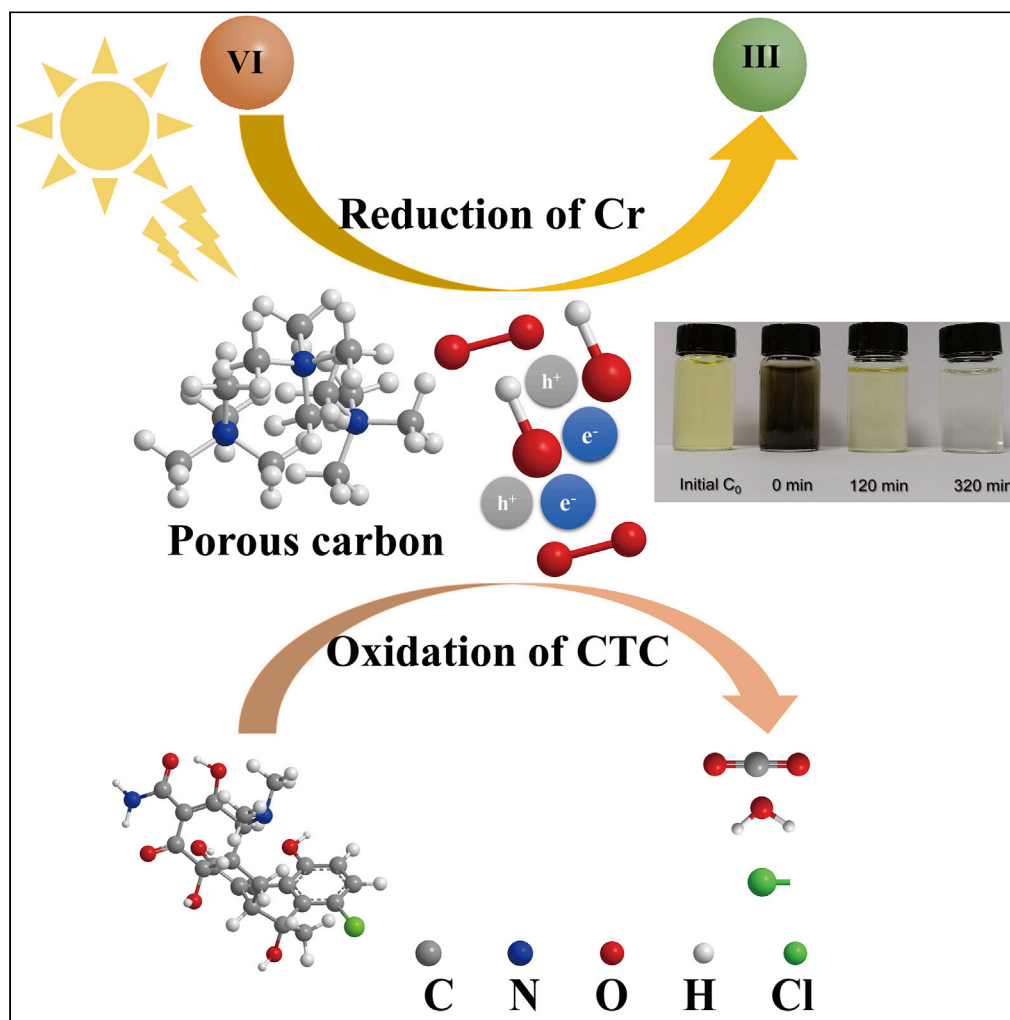**Article**

# Biomass waste-derived porous carbon efficient for simultaneous removal of chlortetracycline and hexavalent chromium



Kai Yan, Ruiqi Li,
Zhiyu Yang, Xin Li,
Yuchen Wang,
Guosheng Wu

yank9@mail.sysu.edu.cn

Highlights

Two-dimensional N-doped hierarchically porous carbon from straw waste

Simultaneous removal of Cr(VI) and chlortetracycline in visible light

The mechanism and kinetics were investigated using UPLC-MS/MS

Photocatalytic reactions were verified as $h^+$, $e^{-1}$, $\cdot OH$, and $\cdot O_2^-$

## Article

# Biomass waste-derived porous carbon efficient for simultaneous removal of chlortetracycline and hexavalent chromium

Kai Yan,[1,3,*] Ruiqi Li,[1] Zhiyu Yang,[1] Xin Li,[1] Yuchen Wang,[1] and Guosheng Wu[2]

## SUMMARY

**The simultaneous removal of mixed containments of antibiotics and heavy metals is still a big challenge in wastewater treatment. Herein, we report the successful synthesis of N-doped porous carbon (abbreviated as NC) from straw waste through the Maillard reaction to activate $sp^3$-$sp^2$ conversion efficient for the simultaneous removal of chlortetracycline (CTC) and hexavalent chromium (Cr(VI)). In 200 min, 96.9% of Cr(VI) was reduced into Cr(III) and 93.1% of CTC was oxidatively degraded. Reactive substances (e.g., $h^+$, $e^{-1}$, $\cdot OH$, and $\cdot O_2^-$) were verified for the photocatalytic reactions. Besides, the possible degradation intermediates of CTC were analyzed with ultra performance liquid chromatography-mass spectrometry (UPLC-MS/MS), and the mechanism of photocatalytic degradation of CTC was then proposed. The synthesized bifunctional NC materials could also be applied for the similar system; this will open the door for promising practical applications.**

## INTRODUCTION

The misuse of antibiotics and the arbitrary release of the sewage containing heavy metal ions have deteriorated the case of water quality (Ye et al., 2019; Zhou et al., 2019; Sun et al., 2020; Yang et al., 2020), which severely menaces the subsistence of aquicolous and terrestrial living body. Chlortetracycline (CTC) with the formula of $C_{22}H_{23}ClN_2O_8$ is a typical antibiotic applied in treating many bacterial and rickettsial infections, which is also frequently utilized in the area of livestock and fish due to its low cost and high efficiency (Wu et al., 2015; Wang et al., 2017, 2020a; Huang et al., 2020). However, due to the very low metabolism and high water solubility of CTC, long-term or a large number use will make an accumulation of CTC in the organism, resulting damage for human or animals (Nguyen et al., 2019; Weng et al., 2019; Zhao et al., 2020; Zhong et al., 2020). Also, because of the random discharge of industrial wastewater, hexavalent chromium (Cr(VI)) has become a main source of heavy metal ions in wastewater pollution (Jin et al., 2016; Zhao et al., 2019; Li et al., 2020). Compared with Cr(III), Cr (VI) with very high toxicity is easy to accumulate in the living body, causing illness or even death in human or animals (Sun et al., 2013; Thacher et al., 2016). More seriously, CTC can combine with Cr(VI) to generate a more complex pollutant that is hard to be degraded (Zhao et al., 2019). Chromium is an essential trace element for animal breeding (promoting metabolism and improving survival rate) (Levina et al., 2016). However, excessive use is extremely harmful, and the abuse of antibiotics in the breeding process adds fuel to the fire. Therefore, how to effectively remove aquaculture wastewater containing both Cr(VI) and CTC is a crucial step in improving the water quality.

More than 10 billion tons of straw-based cellulosic biomass is produced annually in China. Most of them are burned or discarded, generating a large amount of waste and environmental pollution. Rational utilization of straw waste to fabricate carbon materials offers the benefits of abundant renewable sources, eco-friendly property, rich functional groups, and good stability (Hu et al., 2019; Wang et al., 2019; Chen et al., 2020; Huang et al., 2021). So far, carbon-based photocatalysts with the improved photocatalytic activities have been frequently studied (Li et al., 2019a; Huang et al., 2021). With a typical porous structure, N-doped carbon exhibits a large surface area, much improved electrical conductivity, and rich reaction active sites (Achour et al., 2014; Chen et al., 2020). In addition, a number of studies have shown that the introduction of N into porous frameworks promotes the electron migration and improves the adsorption of pollutants, thus significantly boosting the removal efficiency (Nie et al., 2019; Wang et al., 2020a; Zhang et al., 2020a). Moreover, rich functional groups of N-doped C materials enhance the interaction between semiconductor
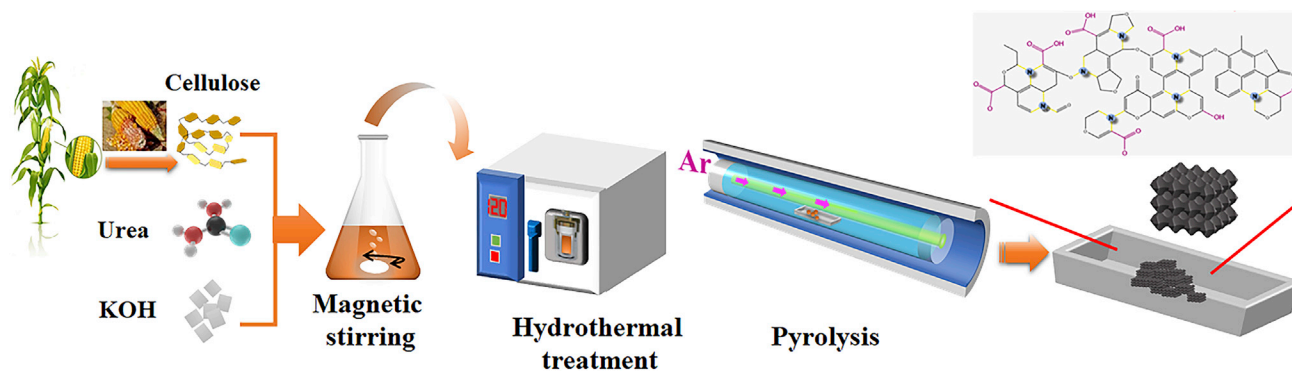
**Figure 1. Schematic of preparing two-dimensional N-doping porous carbon (NC).**

catalysts and pollutants to enhance the stability (Lu et al., 2004; Wang et al., 2020b). Albeit C-based materials and the other catalysts (e.g., MoC/C$_3$N$_4$) have made great progress (Huang et al., 2020; Wang et al., 2020a; Lu et al., 2004), it is still a big challenge to rationally design higher efficient, visible light photocatalysts with multifunctional roles in the photocatalytic oxidative degradation of CTC and removal of Cr(VI).

In this study, we have successfully fabricated two-dimensional N-doped hierarchically porous carbon (NC) using a facile hydrothermal strategy (Figure 1 and supplemental information) from biomass waste straw (cellulose and corn cobs; Figure S1). These bifunctional NC materials are efficient for the selective removal of the mixed CTC and Cr(VI) with high efficiency. The catalytic system has several advantages: (i) high specific surface area as well as hierarchically porous structure can facilitate the contact and provides more access to the internal active space; (ii) the utilization of biomass waste offers a sustainable route to fabricate carbon materials and N doping can improve the electronic conductivity, increasing the amount of active sites; (iii) different types of nitrogen species (e.g, pyridinic-, pyrrolic-, and graphitic-N) can facilitate the adsorption capacity of CTC and Cr(VI) through hydrogen bonding and $\pi$-$\pi$ stacking interactions. (iv) NC materials exhibit high efficiency and stability for the simultaneous removal of CTC and Cr(VI).

## RESULTS AND DISCUSSION

### Characterizations of the as-prepared photocatalyst

X-ray diffraction (XRD) patterns of the synthesized NC from cellulose and corn stalk are shown in Figures 2A and 2B, respectively. The broad peak position located at 2θ of ~23° and the weak peak sat at 2θ of ~43° can be assigned to the degree of stacking order of the layered carbon structure (002) and ordered hexagonal carbon structure (100) planes, respectively. This indicated the low crystallinity degree and the presence of amorphous carbons. Besides, the weak peak at 17.5° was highly possible due to the formation of C$_3$N$_4$ (Wang et al., 2019; Hu et al., 2020). Fourier transform infrared spectroscopy (FTIR) spectra were then applied to explore the chemical bond and functional groups on the surface. The fabricated both NC samples contain rich oxygen functional groups. Figures 2C and 2D showed that the broad peak at 3300–3550 cm$^{-1}$ was O–H stretching from the water molecules adsorbed and phenolic hydroxyl. Peaks at 1060–1170 cm$^{-1}$, 1380 cm$^{-1}$, 1620–1720 cm$^{-1}$, and 2350 cm$^{-1}$ were the vibrations induced by C-O, O=C-O, C=O, and O=C=O bonds, respectively (Huang et al., 2010; Yan et al., 2013; Cheng et al., 2019), suggesting sp$^2$-hybridized carbon in oxygen functional groups. Besides, NC materials fabricated from corn cobs exhibit weak peaks at 1320 cm$^{-1}$ and 1434 cm$^{-1}$ from C-N vibration, confirming that the N-(C)$^3$ structure existed.

The Brunauer-Emmett-Teller (BET) surface area and porosity information of the synthesized NC samples are analyzed by N$_2$ adsorption-desorption tests (Figure 3). The BET specific surface area of NC from cellulose is calculated to be ~178 m$^2$/g. In comparison, the NC synthesized from corn cobs has much larger surface area of ~325 m$^2$/g. This was possible as the plant itself has a naturally optimized multi-channel structure and abundant functional groups, and at the same time, it promotes pore formation with the aid of a KOH activator (Li et al., 2014). Thus, a porous carbon material with a larger specific surface area was obtained. The isotherm curve of NC synthesized from corn cobs shows the typical IV curve with a hysteresis loop, confirming that the NC possesses a number of mesoporous structures which existed in the NC
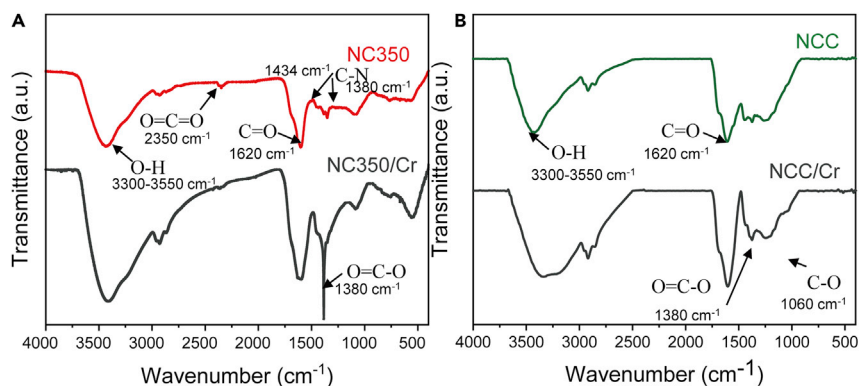
**Figure 2. FTIR of NC synthesized from (C) cellulose and (D) corn cobs.**

samples. Pore size dispersion calculated from the Barrett-Joiner-Halenda method indicates a relatively narrow distribution (mainly around 5 nm). The synthesized NC materials with large surface area and high porosity are considered as attractive candidates for adsorption or photocatalysis. Besides, the large surface area and pore structure are beneficial for electrolyte permeation and enhancement of ion diffusion, improving the photocatalytic activities.

Raman spectra were then utilized to further study the defect structure of N-doped carbon samples. As shown in Figures 4A and 4B, the clear D and G bands are observed. It can be seen that both D band peak ($\sim$1345 cm$^{-1}$) and G band peak ($\sim$1593 cm$^{-1}$) are presented in the samples. The D band can be assigned to the disorder originating from sp3 carbons which indicates successful introduction of defects by N doping. The G band was associated with a hexagonal carbon structure, and the intensity ratio of the D band ($\sim$1345 cm$^{-1}$) to the G band ($\sim$1593 cm$^{-1}$) ($I_D/I_G$) was around 1.10 which was very similar to that of graphene oxide reported by the literature (Tang et al., 2015; Wang et al., 2019). In addition, Raman spectrum (Figure 4B) indicates that NC fabricated from corn cobs has lots of defects, which is likely due to the internal structure of corn cobs. The distance between D and G bands of NC fabricated from corn cobs
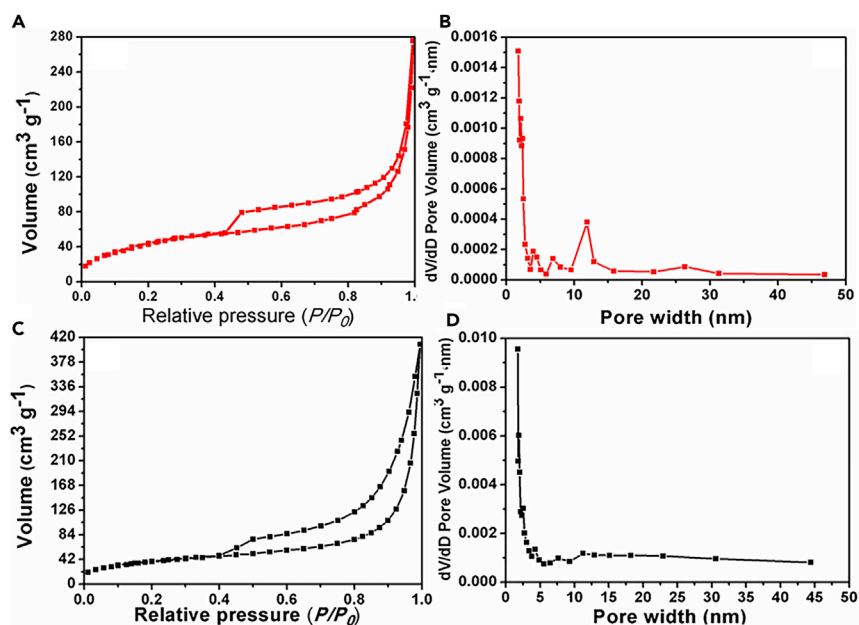


**Figure 3. N$_2$ adsorption-desorption isotherm curves and pore size dispersion of NC from (A, B) cellulose and (C, D) corn cobs.**
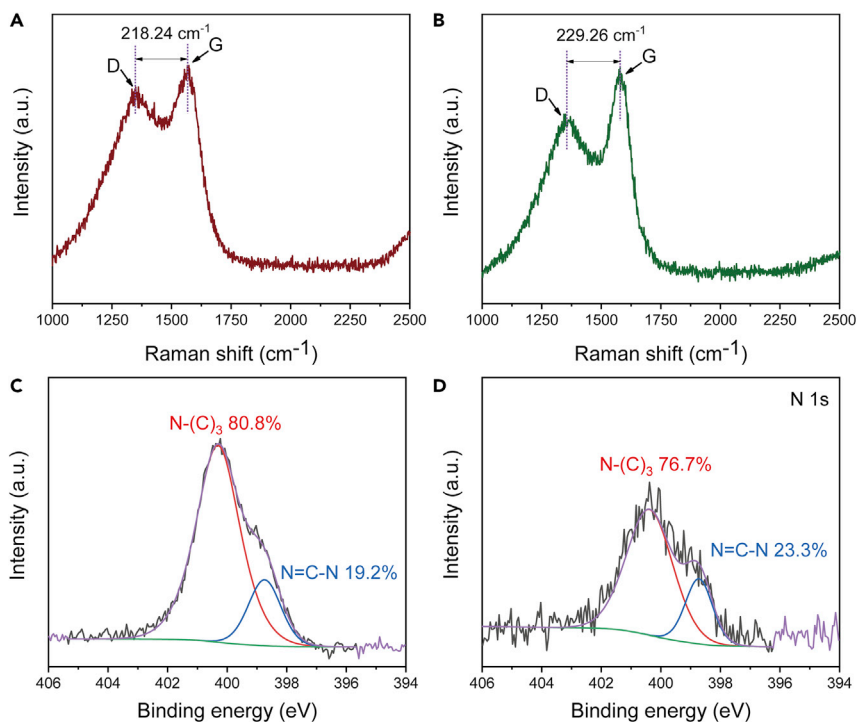
**Figure 4. Raman spectra and high-resolution N 1s XPS analysis spectra of NC fabricated from (A, C) cellulose and (B, D) corn cobs.**

(Figure 4B) has larger distance than that of the material prepared from cellulose (Figure 4A). X-ray photoelectron spectroscopy (XPS) analysis was further carried out to investigate the covalent state of N and C elements in the NC samples (Figures 4C and 4D). The N1s spectra hold two peaks (398.6 ± 0.1 and 400.3 ± 0.2 eV), assigning to pyridinic N (28.8 at%) as well as pyrrolic N (14.7 at%) and corresponding to C=N-C and N-(C)3, respectively. This information suggested that the nitrogen atoms were successfully doped into the porous carbon and N-(C)3 was dominant compared to the ratio of these two structures. Carbon and nitrogen have similar atom diameters, favoring the atom replacement. Besides, pyridinic N and pyrrolic N are often reported as active centers for the photo-enhanced adsorption. Therefore, the high amount of pyridinic N and pyrrolic N in NC samples synthesized from carbon cobs could contribute to the desirable photocatalytic activities.

The surface morphology of the two NC samples is shown in Figure S2. Scanning electron microscopy (SEM) images show the interconnected porosities existing in two carbon samples. In Figures S2A and S2B, samples prepared using cellulose showed clear aggregation of layers, while in Figures S2C and S2D, NC samples synthesized from corn cobs presented the enlarging porosities. The pore size ranged around tens of nanometers. As previously reported (Dong et al., 2021; Wang et al., 2019), carbon particles would gradually fuse together and then form larger aggregates at the pyrolysis temperature. The typically textural structure of NC samples is studied by transmission electron microscopy (TEM), as shown in Figure 5. The obtained NC exhibits large porosity, and the pore sizes ranged from dozens to hundreds of nanometers. Figure 5A displays the layers with the clear aggregation, and the amorphous structure was observed at high magnification (Figure 5B). The typical amorphous carbon existed as the distorted lattice fringes, in which there were plentiful micropore structures. Figure 5C shows the thin carbon layers with wrinkles. The higher magnification TEM image (Figure 5D) shows the interconnected porosity that is made of abundant 2–5-nm mesopores linked by 3–5 graphitic layers with the obscure worm-like fringes. These porous structures can not only provide high specific surface area but also offer a 3D interconnected conductive substance (matrix) which is beneficial for ion and electron transport.

## Photocatalytic reduction of Cr (VI) using NC fabricated from cellulose

The experimental design was performed using analysis of variance (Yan et al., 2013; Brown and Wright, 2014; Zarrinbakhsh et al., 2014; Li et al., 2019b). The details of model parameters are shown in supplemental
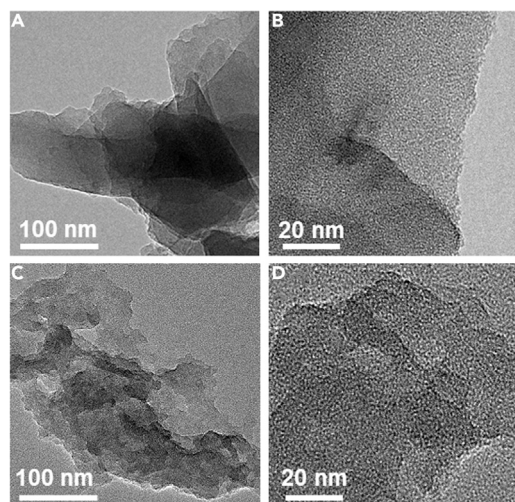
**Figure 5. TEM images of NC materials fabricated from (A and B) cellulose and (C and D) corn cobs.**

information. Important reaction parameters containing two-factor interactions can be verified through the measured p values. Besides, the gaps between the predictions and actual values can be generated to show the quality of the model. To better evaluate many reaction parameters to identify the key factor and their interactions, a two-level factorial model was utilized according to the previous tests. In the two-level factorial design, one upper and one lower value of each factor was chosen: initial concentration of Cr(VI), catalyst amount, and intensity of visible light. The actual composite design was shown in Figure S3, and the actual experimental runs were shown in Table S2.

Based on the 20 runs, Figure 6 shows the experimental values compared with the theoretically predicted data. A very small gap between predicted and practical values was observed, which indicated that the model can predict the experiment very well. Figure 7 describes the interaction of two factors on the removal efficiency of Cr(VI). Figures 7A and 7B show the influence of the initial concentration of Cr(VI) and catalyst amount on the total removal efficiency. When the light intensity was 30 mW/cm$^2$, the removal amount increased when the catalyst amount decreased (Figure 7A). Besides, the initial concentration has more significant effect on the total removal efficiency of Cr(VI). The contour map is an approximate ellipse, indicating that the interaction of the initial concentration of Cr(VI) and catalyst amount is strong on the total removal efficiency. Figures 7C and 7D display the effect of the initial concentration of Cr(VI) and light intensity on the removal efficiency. When the catalyst amount was 15 mg, the light intensity can promote the reaction and enhance the removal of more Cr(VI). Figures 7E and 7F describe the mutual effect of catalyst amount and visible light intensity on the reaction. The model identified that the light intensity has less effect in comparison with the catalyst amount.
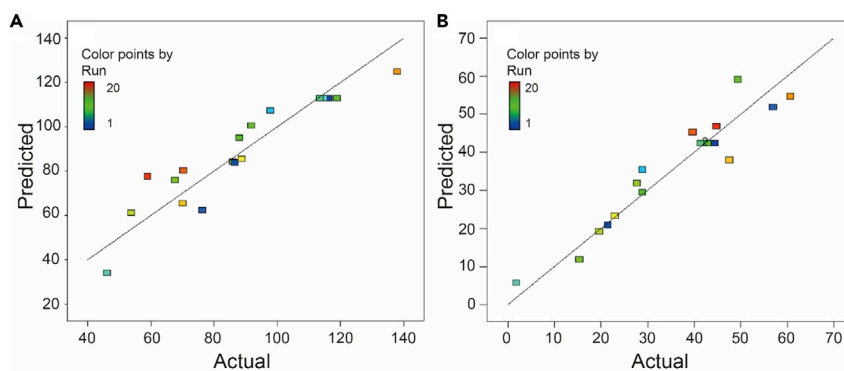


**Figure 6. The comparison between the predicted and actually experimental values**
(A and B) (A) The theory predicted the total removal capacity vs the actual values from experiments and (B) the photoremoval capacity vs the actual values.
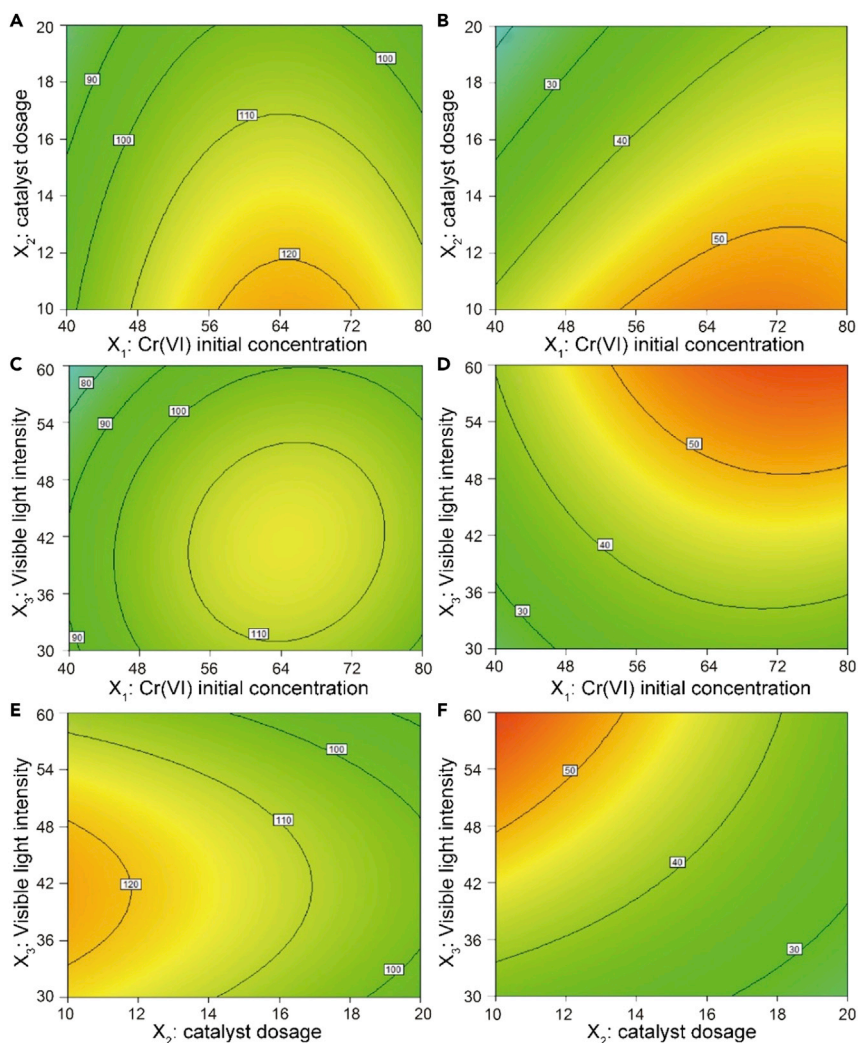
**Figure 7. Effect of (A) $X_1X_2$, (C) $X_1X_3$, and (E) $X_2X_3$ on $Q_{tot}$; Effect of (B) $X_1X_2$, (D) $X_1X_3$, and (F) $X_2X_3$ on the removal efficiency of Cr(VI). Reaction note: $X_1$: initial concentration of Cr(VI); $X_2$: catalyst amount; $X_3$: light intensity.**

## Photocatalytic removal of Cr(VI) by NC from corn cobs

Based on the aforementioned work, we utilize the optimal conditions (e.g., 40 mg/L Cr(VI), 50 mL, pH of 2.0, 20 mg carbon catalyst, the adsorption time of 120 min, and the illumination time of 200 min) to further investigate the photocatalytic removal of Cr(VI) using the NC fabricated from corn cobs. As shown in Figure S4, it is clear to see that NC fabricated from corn cobs could efficiently remove the Cr(VI), and ~88% was removed in 5 hr. The difference between adsorption and photoreduction was shown in Figure 8A. The concentration of Cr(VI) has clear decrease between the adsorption and photoreduction parts. The color change over time was shown in Figure 8B. At 0 min, the black color mainly from the carbon and the transparent solution was reached after 320 min.

## Simultaneous removal of CTC and Cr(VI) by NC fabricated from corn cobs

The photocatalytic evaluation of the synthesized NC fabricated from corn cobs was studied by photocatalytic oxidative degradation of CTC and photocatalytic reduction of Cr(VI). As shown in Figure S5, 6 mg/L CTC reached the adsorption-desorption equilibrium in the dark for 120 min. Before the light irradiation, adsorption experiments were performed under dark conditions, and the data were shown in Figure 9. It was clear to see that the concentrations of CTC and Cr(VI) changed after 30 min, and nearly no obvious
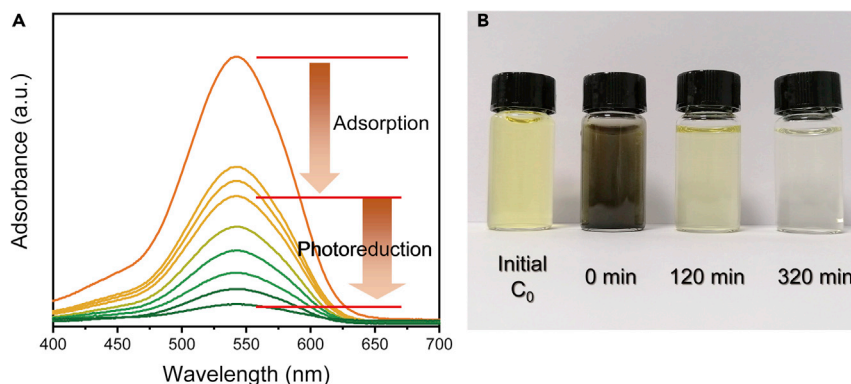
**Figure 8. Adsorption and photoreduction of Cr(VI) by NC fabricated from (A) corn cobs; (B) pictures of solution color change over time.**

decrease was observed after 120 min, indicating that an adsorption-desorption equilibrium reached in the dark for 120 min. It was worth noting that different concentrations of CTC and Cr(VI) showed the similar trend. The irradiated experiments of CTC and Cr(VI) solution were then continuously carried out for 200 min. Figure 9A shows the change of Cr(VI) concentration versus reaction time at pH of 2.0 in 50 mL solution using 5 mg NC catalyst. The adsorption capacity of Cr(VI) for 6 samples containing different CTC concentrations (0, 6, 8, 10, 12, 14 mg/L) using NC reached 36.3–40.4% in 120 min, indicating that the adsorption of Cr(VI) was not significantly influenced by different CTC concentrations. The photoreduction of Cr(VI) was greatly enhanced, and the concentration of Cr(VI) decreased greatly under light irradiation. When no CTC was added, the removal efficiency of Cr(VI) was 71.4% at 320 min. When the CTC concentration was increased to 6 mg/L, the efficiency increased to 87.6%. Further increasing CTC, more Cr(VI) was removed. When the CTC concentration was 14 mg/L, the efficiency reached 96.9% in 320 min. Reaction constant was then calculated to be 0.0010, 0.0015, 0.0016, 0.0017, 0.0018, and 0.0019 $min^{-1}$ when the concentration of CTC was increased from 0 to 14 mg/L, suggesting that more photoreduction of Cr(VI) occurred when CTC increased. This was due to the fact that CTC would consume the photogenerated hole and enhance the separation of photogenerated hole vs electron, promoting the photoreduction of Cr(VI). Figure 9B depicted the change of CTC with reaction time at the fixed amount of Cr(VI) with the concentration of 12 mg/L. When the CTC concentration was 6 mg/L, the adsorption efficiency was 37.8%. While the CTC concentration was increased to 8, 10, and 12 mg/L, the adsorption efficiency decreased to 35.9%, 31.8%, and 21.8%, respectively, in 120 min. When light irradiation started, the various concentrations of CTC started to degrade. After 200 min, the removal efficiency was 93.1%, 81.6%, 79.6%, 68.5%, and 50.4%.

### Photocatalytic degradation intermediates of CTC

After light irradiation, a series of intermediates could be produced as the photocatalytic degradation of CTC occurred (Figure S6). According to previous works (Wang et al., 2020a; Zhang et al., 2020b), the
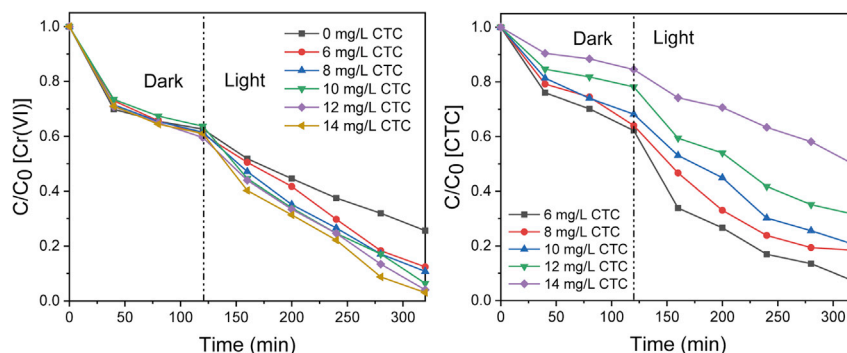


**Figure 9. Simultaneous removal of different concentrations of CTC with Cr(VI) by NC fabricated from corn cobs under the conditions of pH = 2.0, 50 mL, 5 mg catalyst.**
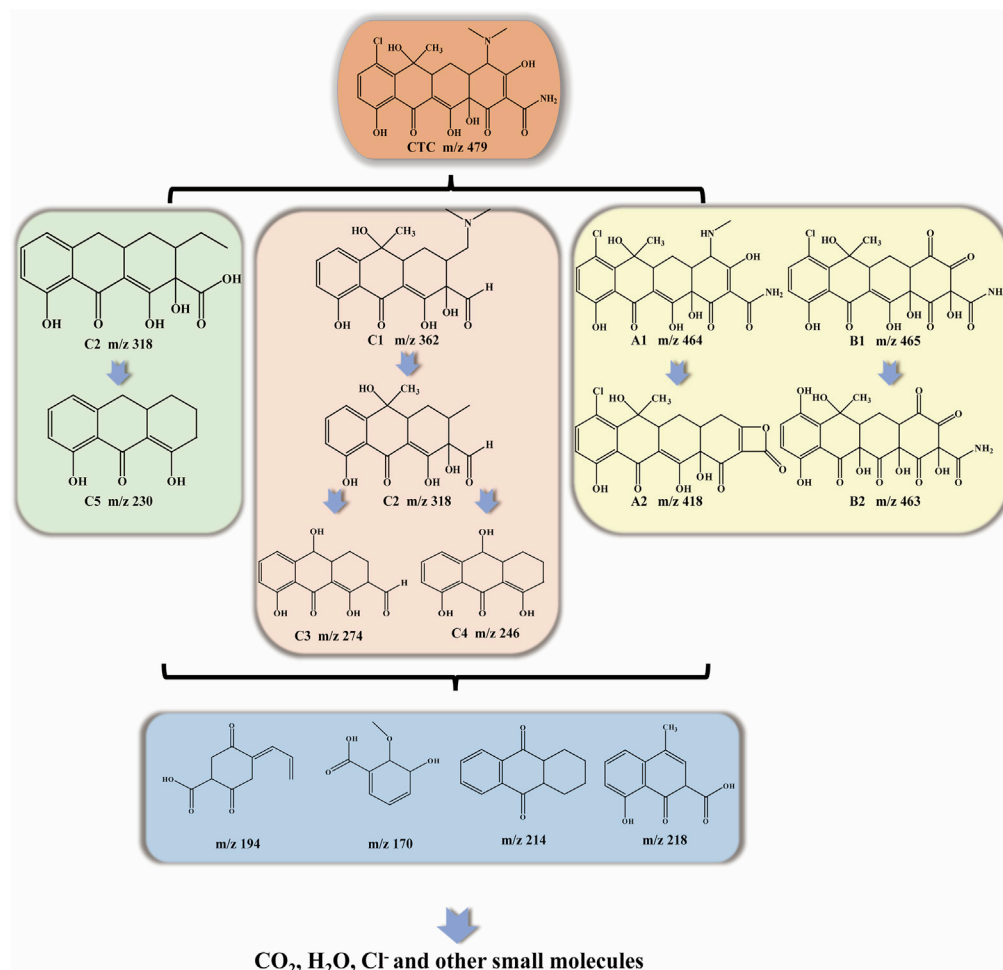
**Figure 10. The degradation mechanism of CTC using NC fabricated from corn cobs.**

decomposing pathway of CTC was divided into three parts in this work, as shown in Figure 10. In pathway I, the CTC molecule was converted to C1 (m/z 362) via a series of reactions including deamination, dechlorination, and dealcoholization. The as-produced C1 would be further degraded to C2 (m/z 318) due to the C-N bond cleavage resulting in the dimethylamino group removed. Under the attack of ·OH or ·$O_2^-$, C3 (m/z 274) and C4 (m/z 246) could further be obtained by the demethylation and deformaldehyde process of C2 (Zheng and Zhang, 2018). For pathway II, the similar degradation process to pathway I of CTC occurred to form smaller molecules (C5 m/z 318) with a tricyclic structure via the open-ring reaction, dichlorination, etc. After that, the ethyl and carboxyl of C5 are further oxidized to produce C6 (m/z 230) (Kong et al., 2020). In addition, the ketone substitution of the dimethylamino moiety in the CTC molecule was pathway III, which could form C7 (m/z 465) by this way. Subsequently, C7 was oxidized to C8 via the hydroxylation process to replace the Cl atom. Ultimately, all the above intermediate products would be decomposed to the small molecule intermediates such as (C9 m/z 194, C10 m/z 170, C11 m/z 214, C12m/z 218) and further mineralized to $CO_2$, $H_2O$, and other inorganic anions.

Total organic carbon (TOC) concentration was detected after the photocatalysis process was completed. According to TOC results, 54.6% of the carbon content in the CTC antibiotic solution could be mineralized on NC catalyst under 190 min of the simulated sunlight irradiation. To study the stability of the prepared NC catalyst from corn cobs, the spent NC catalyst was recycled, washed by pure ethanol, dried in the Ar protecting oven, and then utilized for the next run. Overall, the stable performance (Figure S7) was obtained, and very slight decrease in degradation performance was mainly due to the inevitable catalyst loss during the recovery process and the potential deactivation of the catalyst surface caused by the degraded
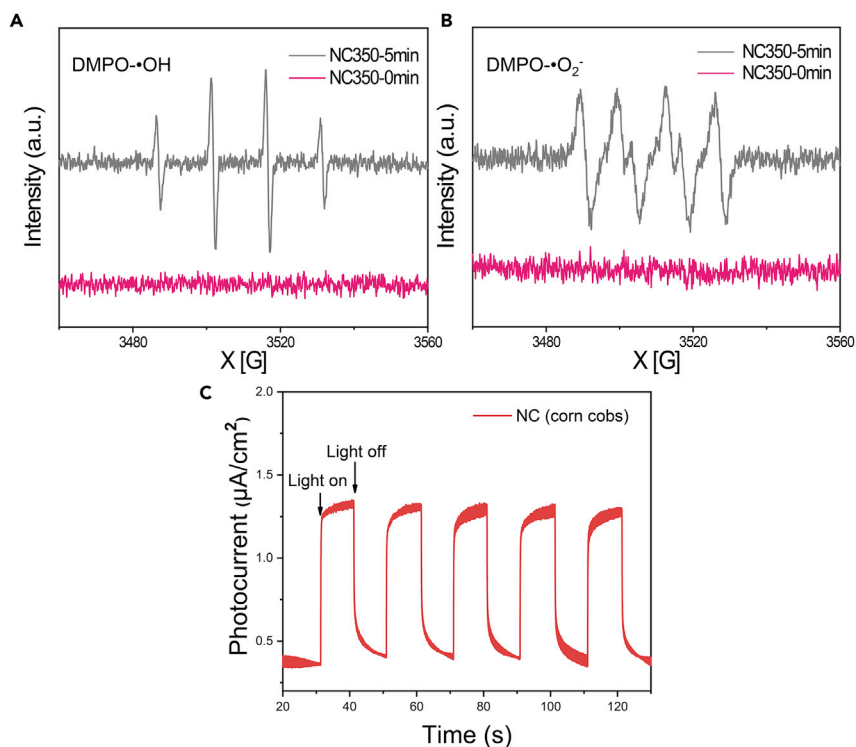
**Figure 11. EPR spectra for (A) ·O$_2^-$ and (B) ·OH in the presence of DMPO, (C) the photocurrent curve under dark/light irradiation condition. Operational parameters: 10 ppm DMPO, 0.1 g L$^{-1}$ catalyst, 6 mg/L CTC, pH of 7, 25°C.**
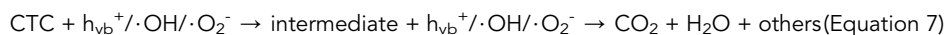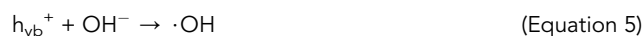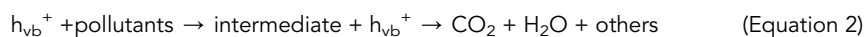
intermediate residues. The XRD pattern of the spent NC showed the similar diffraction peak at 2θ = 26° and 44° meaning the stable crystal structure of the NC (Figure S8). XPS spectrum analysis of the used NC from corn cobs illustrates that it consisted of C, O, and N. Moreover, the XPS spectrum of the NC after the reaction proved the existence of Cr (Figure S9). The N1s spectra (Figure S10) confirmed the pyridinic N and pyrrolic N with the close values of the fresh NC sample. Moreover, after the reaction, the SEM morphology of the NC still maintained obvious porous structure (Figure S11), indicating the stable structure.

### Photocatalytic degradation mechanisms

In order to identify the main active substances that affect CTC degradation and Cr(VI) reduction, we used p-benzoquinone (BPQ), EDTA disodium salt dihydrate (EDTA-2Na), and tert-butanol (TBA) as quenchers for ·O$_2^-$, h$^+$, and ·OH to perform quenching experiments. Compared with the blank control, the process of CTC removal was hindered to varying degrees after the scavengers were added (Figure S12). Among them, the BPQ exhibited the intensive inhibition of 44% for CTC degradation, which might ascribe to the large amount of ·O$_2^-$ formed in the photocatalytic process. Moreover, both of EDTA-2Na and TBA performed the hindrance effect for CTC degradation resulting ~16% degradation efficiency decreasing. These results indicated the existence of ·OH and photogenerated h$^+$, both of which could make some contribution for CTC removal. In addition, the photogenerated holes (h$^+$) and electrons (e$^-$) existed in pairs. The generation of h$^+$ was normally accompanied by e$^-$ generation, which was conductive to reducing Cr(VI) to Cr(III). The synergetic photocatalytic degradation and reduction mechanism of CTC and Cr(VI) was depicted in Figure S13.

To further confirm the reaction mechanism, electron paramagnetic resonance (EPR) was applied to prove the presence of active substances using 5,5-dimethyl-1-pyrroline N-oxide (DMPO) as the capture agent. As shown in Figures 11A and 11B, there were no radical characteristic peak appearances without light irradiation. On the contrary, the standard quadruple and sextuple characteristic peaks of DMPO-·OH and DMPO-·O$_2^-$ appeared under the visible light irradiation, in which the peak height ratio of DMPO-·OH was 1:2:2:1, and the main peak height ratio of DMPO-·O$_2^-$ was 1:1:1:1. Furthermore, the peak intensity

could reflect the amount of corresponding radicals. From the obviously higher peak intensity in Figure 11, it indicated that a large amount of ·OH and ·$O_2^-$ were produced. All of the above results were consistent with the scavenger experiment and further confirmed the dominant contribution of ·OH and ·$O_2^-$ for CTC degradation. From the photocurrent curve of NC catalyst (Figures 11C), the current density increased significantly under the simulated natural light compared with the dark condition, which further illustrated the generation of photogenerated carriers (Equation (1)). The as-generated $h^+$ and $e^-$ could directly oxide pollutants and reduce Cr(VI), respectively (Equations (2) and (3)). Furthermore, the $h^+$ and $e^-$ could react with $H_2O$, $OH^-$, and $O_2$ to form ·OH and ·$O_2^-$ (Equations (4), (5), and (6)). Depending on these reactive substances, the CTC and Cr (VI) could be effectively oxidized and reduced (Equation (7)).

$$\text{Photocatalyst (NC)} + h\nu \rightarrow h_{vb}^+ + e_{cb}^- \qquad \text{(Equation 1)}$$

$$h_{vb}^+ + \text{pollutants} \rightarrow \text{intermediate} + h_{vb}^+ \rightarrow CO_2 + H_2O + \text{others} \qquad \text{(Equation 2)}$$

$$\text{Cr (VI)} + e_{cb}^- \rightarrow \text{Cr (III)} \qquad \text{(Equation 3)}$$

$$h_{vb}^+ + H_2O \rightarrow H^+ + \cdot OH \qquad \text{(Equation 4)}$$

$$h_{vb}^+ + OH^- \rightarrow \cdot OH \qquad \text{(Equation 5)}$$

$$e_{cb}^- + O_2 \rightarrow \cdot O_2^- \qquad \text{(Equation 6)}$$

$$\text{CTC} + h_{vb}^+/\cdot OH/\cdot O_2^- \rightarrow \text{intermediate} + h_{vb}^+/\cdot OH/\cdot O_2^- \rightarrow CO_2 + H_2O + \text{others} \qquad \text{(Equation 7)}$$

## Conclusions

In conclusion, we have successfully fabricated two-dimensional N-doped hierarchically porous carbon from biomass waste (cellulose and corn cobs) via a facile route. The N-doped hierarchically porous carbon has large surface area, better visible light absorption capacity, the enhanced separation efficiency of $e^-$ and $h^+$, and improved lifetime. NC materials thus presented superior photocatalytic performance for the simultaneous removal of CTC and Cr(VI) compared with the original carbon. After 90 min of visible light irradiation, the removal efficiencies of CTC and Cr(VI) were up to 93.1% and 96.9% by N-doped C semiconductors, respectively. Besides, it can keep the removal efficiency over >90% for both CTC and $Cr^{6+}$ after 5 runs, showing promising prospect in the actual treatment of the simulated wastewater. Free radical capture tests and EPR results demonstrated that main active materials in the photocatalytic oxidation reaction are $h^+$, ·OH, and ·$O_2^-$, while main active species in the reduction reaction of Cr(VI) is $e^-$. UPLC-MS/MS analysis revealed that CTC molecules can be effectively degraded by photocatalysts NC documenting their excellent photocatalytic performance.

## Limitations of the study

We had investigated the porous carbon synthesized from biomass waste for photocatalytic oxidation of CTC and reduction of Cr(VI). Various reaction parameters and mechanism have been studied in this work. However, the actual wastewater containing various antibiotics and heavy metals has not been studied. We will perform the study in the future work.

## METHODS

All methods can be found in the accompanying transparent methods supplemental file.

## SUPPLEMENTAL INFORMATION

Supplemental information can be found online at https://doi.org/10.1016/j.isci.2021.102421.

# iScience
## Article

## AUTHOR CONTRIBUTION

Conceptualization, K.Y. and R.L.; methodology and experiments, R.L., Z.Y., and X.L.; writing, R.L., K.Y., Y.W., and G.W.

## DECLARATION OF INTERESTS

The authors declare no competing financial interest.

## REFERENCES

Achour, A., Ducros, J.B., Porto, R.L., Boujtita, M., Gautron, E., Brizoual, L., Djouadi, M.A., and Brousse, T. (2014). Hierarchical nanocomposite electrodes based on titanium nitride and carbon nanotubes for micro-supercapacitors. Nano Energy 7, 104–113.

Brown, T.R., and Wright, M.M. (2014). Techno-economic impacts of shale gas on cellulosic biofuel pathways. Fuel 117, 989–995.

Chen, Z., Zhang, M., Wang, Y., Yang, Z., Hu, D., Tang, Y., and Yan, K. (2020). Controllable synthesis of nitrogen-doped porous carbon from metal-polluted miscanthus waste boosting for supercapacitors. Green. Energy Environ. https://doi.org/10.1016/j.gee.2020.07.015.

Cheng, W., Zhao, X., Su, H., Tang, F., Che, W., Zhang, H., and Liu, Q. (2019). Lattice-strained metal–organic-framework arrays for bifunctional oxygen electrocatalysis. Nat. Energy 4, 115–122.

Dong, Z., Zhang, L., Gong, J., and Zhao, Q. (2021). Covalent organic framework nanorods bearing single Cu sites for efficient photocatalysis. Chem. Eng. J. 430, 126383.

Hu, D., Xu, H., Yi, Z.X., Chen, Z., Ye, C.L., Wu, Z.T., Garces, H.F., and Yan, K. (2019). Green $CO_2$-assisted synthesis of mono- and bimetallic Pd/Pt nanoparticles on porous carbon fabricated from sorghum for highly selective hydrogenation of furfural. ACS Sustain. Chem. Eng. 7, 15339–15345.

Hu, K., Li, R., Ye, C., Wang, A., Wei, W., Hu, D., Qiu, R., and Yan, K. (2020). Facile synthesis of Z-scheme composite of $TiO_2$ nanorod/g-$C_3N_4$ nanosheet efficient for photocatalytic degradation of ciprofloxacin. J. Clean. Prod. 253, 120055.

Huang, C., Zhang, C., Huang, D., Wang, D., Tian, S., Wang, R., Yang, Y., Wang, W., and Qin, F. (2021). Influence of surface functionalities of pyrogenic carbonaceous materials on the generation of reactive species towards organic contaminants: a review. Chem. Eng. J. 404, 127066.

Huang, D., Zhang, Q., Zhang, C., Wang, R., Deng, R., Luo, H., Li, T., Li, J., Chen, S., and Liu, C. (2020). Mn doped magnetic biochar as persulfate activator for the degradation of tetracycline. Chem. Eng. J. 391, 123532.

Huang, S., Peng, H., Tjiu, W.W., Yang, Z., Zhu, H., Tang, T., and Liu, T. (2010). Assembling exfoliated layered double hydroxide (LDH) nanosheet/carbon nanotube (CNT) hybrids via electrostatic force and fabricating nylon nanocomposites. J. Phys. Chem. B 114, 16766–16772.

Jin, W., Du, H., Yan, K., Zheng, S.L., and Zhang, Y. (2016). Improved electrochemical Cr(VI) detoxification by integrating the direct and indirect pathways. J. Electroanal. Chem. 775, 325–328.

Kong, W., Gao, Y., Yue, Q., Li, Q., Gao, B., Kong, Y., Wang, X., Zhang, P., and Wang, Y. (2020). Performance optimization of CdS precipitated graphene oxide/polyacrylic acid composite for efficient photodegradation of chlortetracycline. J. Hazard. Mater. 388, 121780.

Levina, A., Pham, T.H.N., and Lay, P.A. (2016). Binding of Chromium(III) to transferrin could be involved in detoxification of dietary Chromium(III) rather than transport of an essential trace element. Angew. Chem. Int. Ed. 55, 8104–8107.

Li, J., Michalkiewicz, B., Min, J., Ma, C., Chen, X., Gong, J., Mijowska, E., and Tang, T. (2019a). Selective preparation of biomass-derived porous carbon with controllable pore sizes toward highly efficient $CO_2$ capture. Chem. Eng. J. 360, 250–259.

Li, K., Yan, S., Zhong, Y., Pan, W., and Zhao, G. (2019b). Multi-objective optimization of the fiber-reinforced composite injection molding process using Taguchi method, RSM, and NSGA-II. Simulation Model. Pract. Theor. 91, 69–82.

Li, M., Liu, C., Cao, H., Zhao, H., Zhang, Y., and Fan, Z. (2014). KOH self-templating synthesis of three-dimensional hierarchical porous carbon materials for high performance supercapacitors. J. Mater. Chem. A 2, 14844–14851.

Li, R., Hu, D., Hu, K., Hao Deng, M.Z., Wang, A., Qiu, R., and Yan, K. (2020). Coupling adsorption-photocatalytic reduction of Cr(VI) by metal-free N-doped carbon. Sci. Total Environ. 704, 135284.

Lu, A.H., Kiefer, A., Schmidt, W., and Schuth, F. (2004). Synthesis of polyacrylonitrile-based ordered mesoporous carbon with tunable pore structures. Chem. Mater. 16, 100–103.

Nguyen, V.T., Nguyen, T.B., Chen, C.W., Hung, C.M., Huang, C.P., and Dong, C.D. (2019). Cobalt-impregnated biochar (Co-SCG) for heterogeneous activation of peroxymonosulfate for removal of tetracycline in water. Bioresour. Technol. 292, 121954.

Nie, C., Dai, Z., Meng, H., Duan, X., Qin, Y., Zhou, Y., Ao, Z., Wang, S., and An, T. (2019). Peroxydisulfate activation by positively polarized carbocatalyst for enhanced removal of aqueous organic pollutants. Water Res. 166, 115043.

Sun, B., Tian, H.-Y., Zhang, C.-X., and An, G. (2013). Preparation of biomimetic-bone materials and their application to the removal of heavy metals. Alche J. 59, 229–240.

Sun, J., Liao, X.P., D'Souza, A.W., Boolchandani, M., Li, S.H., Cheng, K., Luis Martinez, J., Li, L., Feng, Y.J., Fang, L.X., et al. (2020). Environmental remodeling of human gut microbiota and antibiotic resistome in livestock farms. Nat. Commun. 11, 1427.

Tang, C., Wang, H.S., Wang, H.F., Zhang, Q., Tian, G.L., Nie, J.Q., and Wei, F. (2015). Spatially confined hybridization of nanometer-sized NiFe hydroxides into nitrogen-doped graphene frameworks leading to superior oxygen evolution reactivity. Adv. Mater. 27, 4516–4522.

Thacher, R., Ravindran, V., and Pirbazari, M. (2016). Modeling and performance prediction of chromate reduction by iron oxide coated sand in adsorber reactors. Alche J. *62*, 3717–3729.

Wang, A., Zheng, Z., Li, R., Hu, D., Lu, Y., Luo, H., and Yan, K. (2019). Biomass-derived porous carbon highly efficient for removal of Pb(II) and Cd(II). Green. Energy Environ. *4*, 414–423.

Wang, A., Zheng, Z., Wang, H., Chen, Y., Luo, C., Liang, D., Hu, B., Qiu, R., and Yan, K. (2020a). 3D hierarchical $H_2$-reduced Mn-doped $CeO_2$ microflowers assembled from nanotubes as a high-performance Fenton-like photocatalyst for tetracycline antibiotics degradation. Appl. Catal. B Environ. *277*.

Wang, H., Shao, Y., Mei, S., Lu, Y., Zhang, M., Sun, J.-k., Matyjaszewski, K., Antonietti, M., and Yuan, J. (2020b). Polymer-derived heteroatom-doped porous carbon materials. Chem. Rev. *120*, 9363–9419.

Wang, W., Fang, J., Shao, S., Lai, M., and Lu, C. (2017). Compact and uniform $TiO_2$@g-$C_3N_4$ core-shell quantum heterojunction for photocatalytic degradation of tetracycline antibiotics. Appl. Catal. B Environ. *217*, 57–64.

Weng, X., Owens, G., and Chen, Z. (2019). Synergetic adsorption and Fenton-like oxidation for simultaneous removal of ofloxacin and enrofloxacin using green synthesized Fe NPs. Chem. Eng. J. *382*, 122871.

Wu, Q., Li, W., Wu, Y., Zong, G., and Liu, S. (2015). Effect of reaction time on structure of ordered mesoporous carbon microspheres prepared from carboxymethyl cellulose by soft-template method. Ind. Crops Prod. 76, 866–872.

Yan, Kai, Lafleur, Todd, and Liao, Jiayou (2013). Facile synthesis of palladium nanoparticles supported on multi-walled carbon nanotube for efficient hydrogenation of biomass-derived levulinic acid*15* (J. Nanopart. Res.), 1906.

Yan, K., Todd, L., and Liao, J. (2013). Facile synthesis of palladium nanoparticles supported on multi-walled carbon nanotube for efficient hydrogenation of biomass-derived levulinic acid. J. Nanopart. Res. *15*, 1–7.

Yang, R., Zhu, Z., Hu, C., Zhong, S., Zhang, L., Liu, B., and Wang, W. (2020). One-step preparation (3D/2D/2D) $BiVO_4$/$FeVO_4$@rGO heterojunction composite photocatalyst for the removal of tetracycline and hexavalent chromium ions in water. Chem. Eng. J. *390*, 124522.

Ye, J., Liu, J., Huang, Z., Wu, S., Dai, X., Zhang, L., and Cui, L. (2019). Effect of reduced graphene oxide doping on photocatalytic reduction of Cr(VI) and photocatalytic oxidation of tetracycline by ZnAlTi layered double oxides under visible light. Chemosphere *227*, 505–513.

Zhang, C., Zhou, Y., Wang, W., Yang, Y., Zhou, C., Wang, L., Lei, L., He, D., Luo, H., and Huang, D. (2020a). Formation of $Mo_2C$/hollow tubular g-$C_3N_4$ hybrids with favorable charge transfer channels for excellent visible-light-photocatalytic performance. Appl. Surf. Sci. *527*, 146757.

Zarrinbakhsh, N., Defersha, F.M., Mohanty, A.K., and Misra, M. (2014). A statistical approach to engineer a biocomposite formulation from biofuel coproduct with balanced properties. J. Appl. Polym. Sci. *131*, 40443.

Zhang, Q., Jiang, L., Wang, J., Zhu, Y., Pu, Y., and Dai, W. (2020b). Photocatalytic degradation of tetracycline antibiotics using three-dimensional network structure perylene diimide supramolecular organic photocatalyst under visible-light irradiation. Appl. Catal. B Environ. *277*, 119122.

Zhao, H., Tian, C., Mei, J., Yang, S., and Wong, P.K. (2020). Synergistic effect and mechanism of catalytic degradation toward antibiotic contaminants by amorphous goethite nanoparticles decorated graphitic carbon nitride. Chem. Eng. J. *390*, 124551.

Zhao, W., Li, J., Dai, B., Cheng, Z., Xu, J., Ma, K., Zhang, L., Sheng, N., Mao, G., Wu, H., et al. (2019). Simultaneous removal of tetracycline and Cr(VI) by a novel three-dimensional AgI/$BiVO_4$ p-n junction photocatalyst and insight into the photocatalytic mechanism. Chem. Eng. J. *369*, 716–725.

Zheng, J., and Zhang, L. (2018). Rational design and fabrication of multifunctional catalyzer $Co_2SnO_4$-$SnO_2$/GC for catalysis applications: photocatalytic degradation/catalytic reduction of organic pollutants. Appl. Catal. B Environ. *231*, 34–42.

Zhong, Q., Lin, Q., Huang, R., Fu, H., Zhang, X., Luo, H., and Xiao, R. (2020). Oxidative degradation of tetracycline using persulfate activated by N and Cu codoped biochar. Chem. Eng. J. *380*, 122608.

Zhou, L., Li, N., Owens, G., and Chen, Z. (2019). Simultaneous removal of mixed contaminants, copper and norfloxacin, from aqueous solution by ZIF-8. Chem. Eng. J. *362*, 628–637.

**Supplemental information**

**Biomass waste-derived porous carbon**

**efficient for simultaneous removal**

**of chlortetracycline and hexavalent chromium**

Kai Yan, Ruiqi Li, Zhiyu Yang, Xin Li, Yuchen Wang, and Guosheng Wu

# Supporting Information

# Biomass waste derived porous carbon efficient for simultaneous removal of chlortetracycline and hexavalent chromium

Kai Yan, Ruiqi Li, Zhiyu Yang, Xin Li, Yuchen Wang, Guosheng Wu

**TRANSPARENT METHODS**

**Chemicals** Corn cobs collected from Guangzhou were used as the precursors of the N-doped porous carbon, whereas the composition information was shown in Table S1. The crushed powder images were shown in Figure S1. The sieved size was around 0.11 mm in this study. Urea (AR, 99%), NaOH (GR, 95%), EDTA-2Na (AR, 98%), p-benzoquinone (AR, 99%), furfuryl alcohol (AR, 98%) were supplied by Macklin Biochemical co., Ltd. Tert-butanol (TBA, 99.8%) and 4-hydroxy-TEMPO (98%) were purchased from Alfa Aesar and Aladdin respectively. All reagents were used without further purification.

**Catalysts synthesis** The two-dimensional N-doped hierarchically porous carbon (NC) were manufactured by a hydrothermal process followed by calcining at 350 ℃ as depicted in Figure 1. Firstly, 1 g corn cobs or cellulose, 1 g urea and 0.8 g KOH were put into 17 mL mixed solution (15 mL water + 2 mL ethanol) and stirred for 12 h. Afterwards, the mixture was placed in a Teflon-lined vessel for the hydrothermal treatment at 170 °C for 6 h, and then calcined at 350 ℃ for 6 h with the rate of 2 ℃/min in argon atmosphere. After calcination, cooling down to room temperature, and the products were then washed with pure water and ethanol several times.

**Photocatalytic performance** The photocatalytic evaluation of the as-synthesized two types of NC materials was tested by the oxidative degradation of antibiotic CTC and reduction of Cr(VI) under the simulated natural light. In a typical procedure, NC catalyst (30 mg) was put into 50 mL CTC (30 mg/L) and/or Cr(VI) (20 mg/L) solution. The dispersed solution was then placed in a photoreactor (CEL-LB70-3, CEAULIGHT) with a 500 W xenon lamp as a light source. Before the photoreaction, the mixed solution in the quartz tube was magnetically stirred in the

reactor for 2 h under dark conditions to reach adsorption equilibrium. After that, the xenon lamp was turned on, and 1 mL samples were extracted, centrifuged, filtered at regular intervals. The extracted samples were analyzed by high performance liquid chromatography (HPLC, Shimadzu SPD-20A) and total organic carbon analyzer (TOC) for the degradation efficiency and mineralization of CTC during the photocatalytic reaction.

**Free radical capture experiment** In order to determine reactive oxygen species (ROS) are involved in the degradation of CTC, P-benzoquinone, tert-butanol, EDTA-2Na, and TEMPO are used as the scavenger of $O_2^-$, $\cdot OH$, $h^+$, and $_1O_2$ for quenching experiment, respectively. The scavenger was added 5 minutes before the end of the dark reaction. At this time, the antibiotic and the catalyst have reached the adsorption equilibrium, which can effectively prevent the scavenger from being adsorbed by the catalyst. This ensures that the dark reaction process is consistent with the original system. The EPR, Bruker A300) is used to further prove the ROS generated during the photoreaction process.

**UPLC-MS analytical methods** The instrument used for UPLC-MS analysis was the Triple TOF TM5600 High Resolution Trap Mass Spectrometer (SCIEX, USA) is equipped with an electrospray ionization source ESI and an atmospheric pressure chemical ionization source APC. In the degradation process, a certain amount of suspension was gathered by syringe every 5 min up to 30 min. And then the obtained sample was purified by filtering through a 0.22 μm membrane for analysis of concentration and degradated products using high-performance liquid chromatography (HPLC, C18 chromatographic column (5 μm, 250 mm×3.5 mm) with an injection volume of 10 μL at a flow rate of 0.8 mL min$^{-1}$. The composition of the mobile phase was acetonitrile and 0.2 % formic acid solution, the volume ratio was 80:20) and liquid

chromatography-mass spectrometry (LCMS, MSQ PLUS/U3000). The catalyst cycle performance measurement process was the same as the above operation. After each photocatalysis, the solution was filtered to recover the solid catalyst, washed with ultrapure water and ethanol for several times, and placed in a vacuum oven to dry overnight and then for the next experiment.

**Characterization techniques** To analyze the qualitative phase of different ratios of NiCoMn-LDHs/NF, X-ray diffraction (XRD), D/max-2200vpc (RIGAKU, Japan), was applied under the condition of 40 kV and 40 mA with a Cu Kα radiation, scan rate at 10° min$^{-1}$ and 2-Theta degree ranging from 10° to 80°. Electron paramagnetic resonance (EPR, Burker A300) was conducted to determine the vacancies on the surface of the powder catalyst. Raman spectra were measured by Raman spectroscopy (DXR2 XI) with a 532 nm laser excitation. X-ray photoelectron spectroscopy (XPS, Nexsa) was investigated with monochromatic Al Kα X-ray as the excitation source and a pass energy of 40 eV to find the changes of valence on NiCoMn-LDHs/NF after oxidation reaction. Atomic Force Microscope (AFM, NanoManVS) was operated to decide the thickness of the powder catalysts.

**ANOVA analysis** The quality of the obtained models was evaluated by Analysis of Variance (ANOVA). Three statistical significance numbers were chosen to characterize the individual model quality:

1. p-value: to determine whether the model is highly significant ($p < 0.001$), significant ($0.001 < p < 0.01$), limited significant ($0.01 < p < 0.05$) or not significant ($p > 0.05$).

2. Pred. R-squared: model ability to make predictions; is smaller than R-squared but should not be substantial smaller; could also be negative in case of a total unsuitable

model.

3. Ade Precision: measures the signal to noise ratio. A ratio greater than 4 is desirable.

Significant reaction variables including two factors interactions can be identified by the calculated p-values of the individual model terms. Finally, a statement is being made if the model is able to make predictions and as the case may be if better results were achieved in controlled experiments.

**Table S1** The components of corn cobs, related to **Figure 1**.

| Name | Chemical Composition (%) | | | | |
|---|---|---|---|---|---|
| | cellulose | hemicellulose | lignin | ash | others |
| Corn cobs | 37.4 | 32.2 | 17.5 | 2.6 | 10.3 |

**Table S2** Experimental parameters and results, related to **Figure 6**.

| Run | Levels | | | Y₁ | Y₂ |
| | $X_1$ | $X_2$ | $X_3$ | $Q_{tot}$(mg/g) | $Q_{pho}$(mg/g) |
| --- | --- | --- | --- | --- | --- |
| 1 | 60 | 15 | 45 | 75.59 | 29.67 |
| 2 | 60 | 15 | 15 | 57.67 | 14.32 |
| 3 | 60 | 15 | 75 | 50.84 | 38.01 |
| 4 | 60 | 15 | 45 | 76.14 | 29.47 |
| 5 | 80 | 10 | 30 | 65.23 | 19.30 |
| 6 | 60 | 15 | 45 | 76.56 | 28.01 |
| 7 | 20 | 15 | 45 | 30.85 | 1.23 |
| 8 | 60 | 15 | 45 | 75.72 | 27.60 |
| 9 | 60 | 15 | 45 | 76.76 | 29.47 |
| 10 | 60 | 15 | 45 | 79.25 | 28.64 |
| 11 | 40 | 10 | 30 | 58.61 | 19.30 |
| 12 | 80 | 10 | 60 | 61.18 | 33.00 |
| 13 | 40 | 20 | 30 | 45.18 | 10.27 |
| 14 | 80 | 20 | 30 | 57.36 | 18.52 |
| 15 | 40 | 20 | 60 | 35.84 | 13.11 |
| 16 | 60 | 25 | 45 | 59.15 | 15.33 |
| 17 | 100 | 15 | 45 | 46.73 | 31.74 |
| 18 | 60 | 5 | 45 | 72.08 | 40.47 |
| 19 | 80 | 20 | 60 | 46.93 | 26.46 |
| 20 | 40 | 10 | 60 | 39.30 | 29.89 |

**Table S3** The elements composition and contents from the XPS survey, related to **Figure 4**.

| element | contents |
|---------|----------|
| C | 85.52% |
| N | 10.61% |
| O | 3.11% |
| F | 0.76% |

**Figure S1** Images of the powder of corn cobs, related to **Figure 1**.
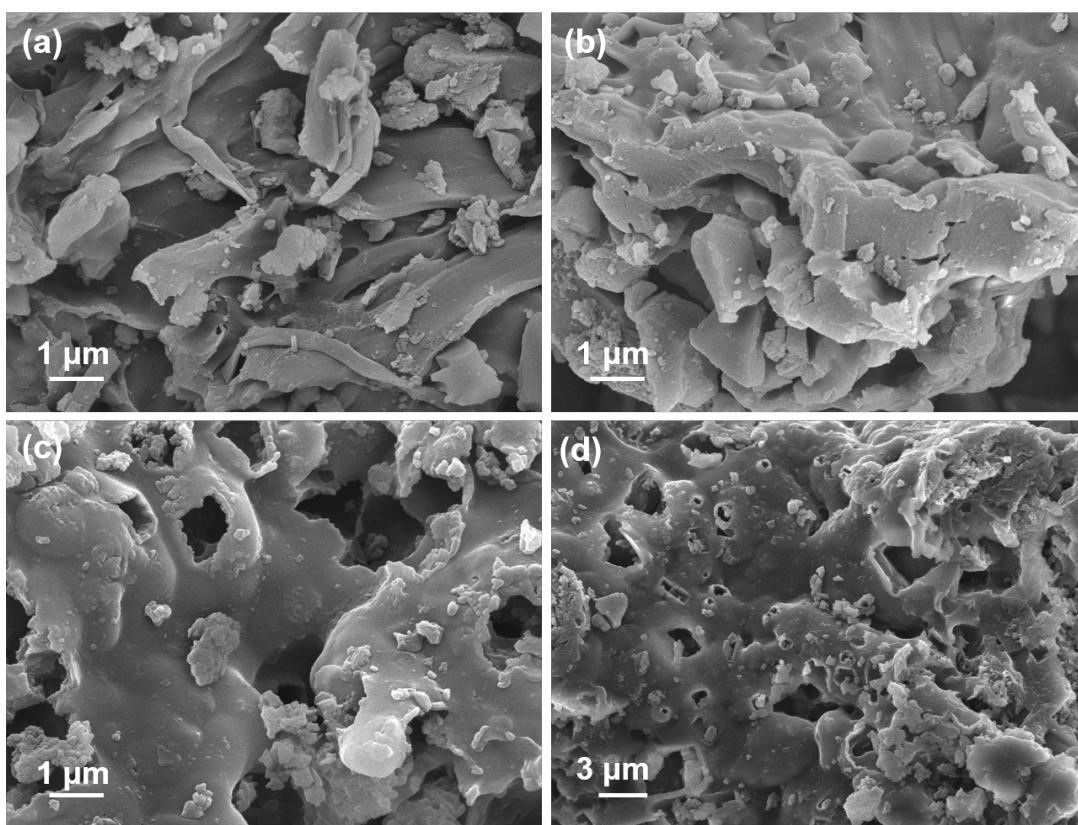
**Figure S2** SEM images of NC from **(a, b)** cellulose and **(c, d)** corn cobs, related to **Figure 5**.

# Central Composite Design

Each numeric factor is varied over 5 levels: plus and minus alpha (axial points), plus and minu
duplicated for every combination of the categorical factor levels.

Numeric Factors: 3 ⌄ (2 to 50)  ◉ Horizontal
Categoric factors: 0 ⌄ (0 to 10)  ○ Vertical

| | Name | Units | Low | High | –alpha | +alpha |
|---|---|---|---|---|---|---|
| A [Numeric] | $C_{(Cr(VI))}$ | mg/L | 40 | 80 | 20 | 100 |
| B [Numeric] | NC amount | mg | 10 | 20 | 5 | 25 |
| C [Numeric] | Visible light | mW/cm2 | 30 | 60 | 15 | 75 |

◉ Enter factor ranges in terms of +/- 1 levels
○ Enter factor ranges in terms of alphas

Type: Full ⌄    Blocks: 1 ⌄

**Points**

Not center points    14
Center points    6

alpha = 2    [Options...]    20 Runs

**Figure S3** The experimental design by the DOE software, related to **Figure 6**.
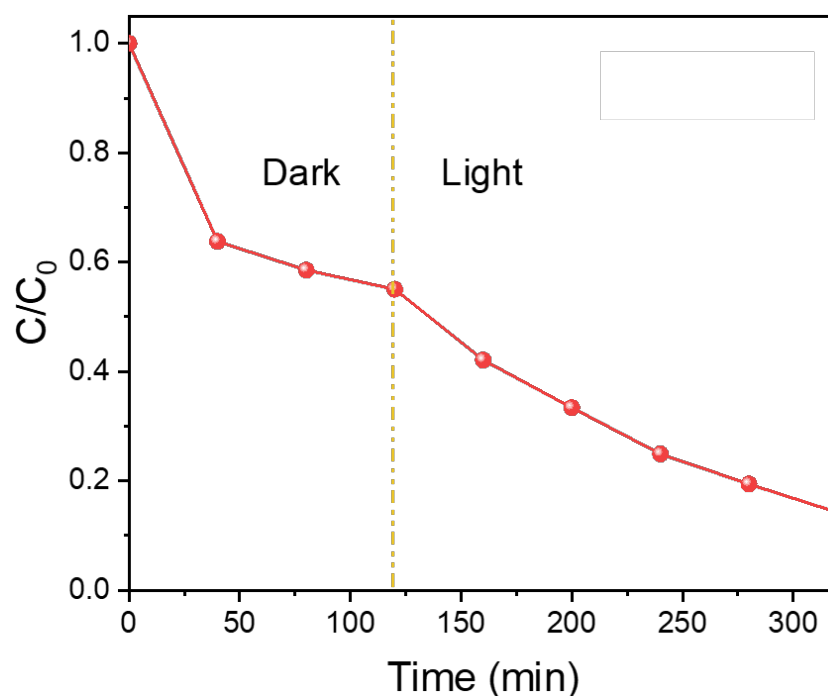
**Figure S4** The adsorption of Cr(VI) by NC synthesized from corn cobs, related to **Figure 8**.
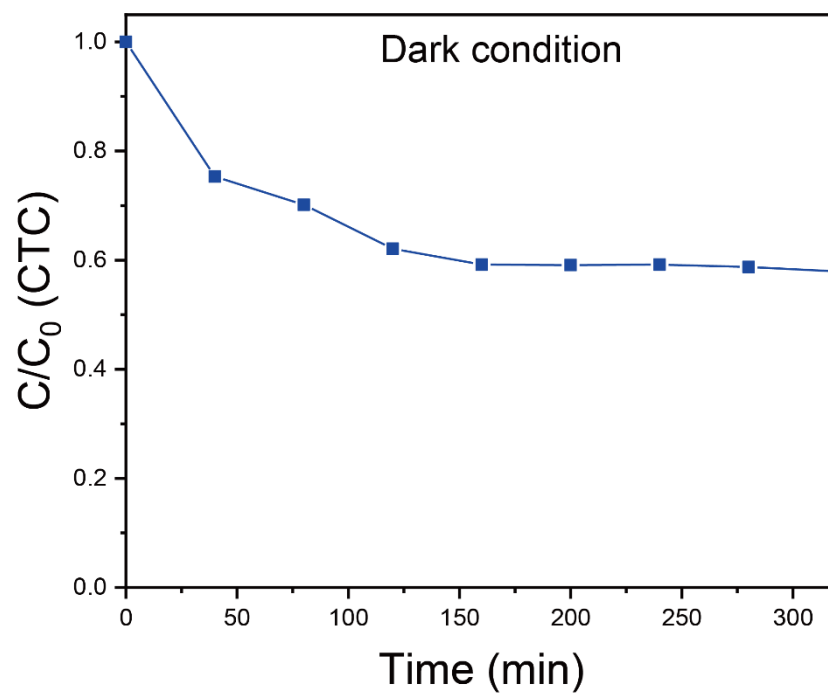
**Figure S5** The adsorption of CTC by NC synthesized from corn cobs under the conditions of pH=2.0, 50 mL 6 mg/L CTC, 5 mg catalyst, related to **Figure 9**.
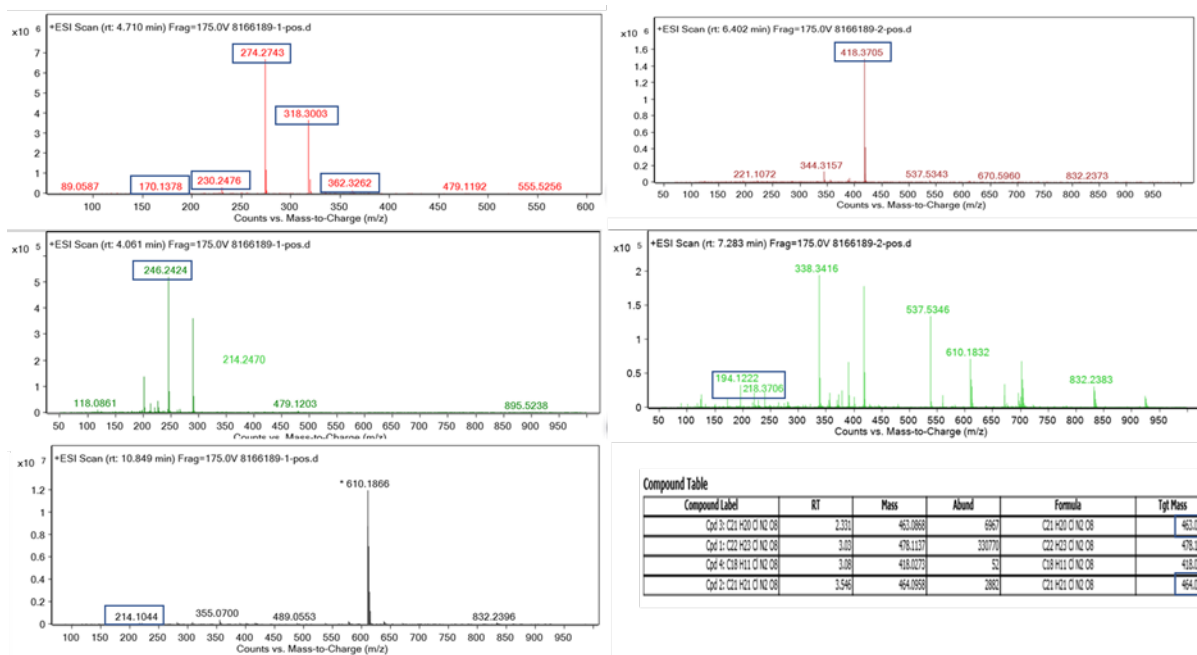
**Figure S6** Mass spectra and proposed structure of detected intermediate products, related to
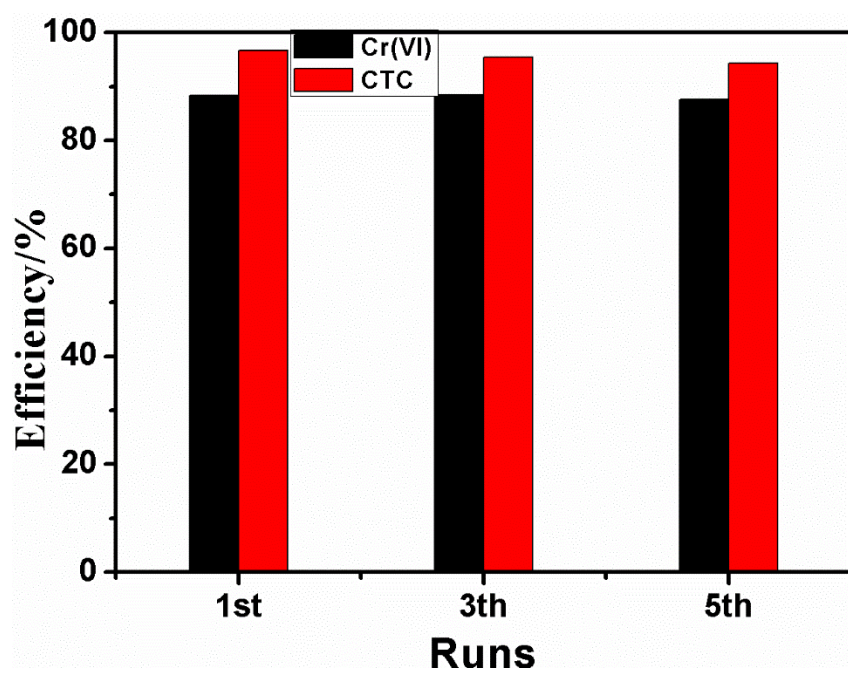
**Figure 10**.

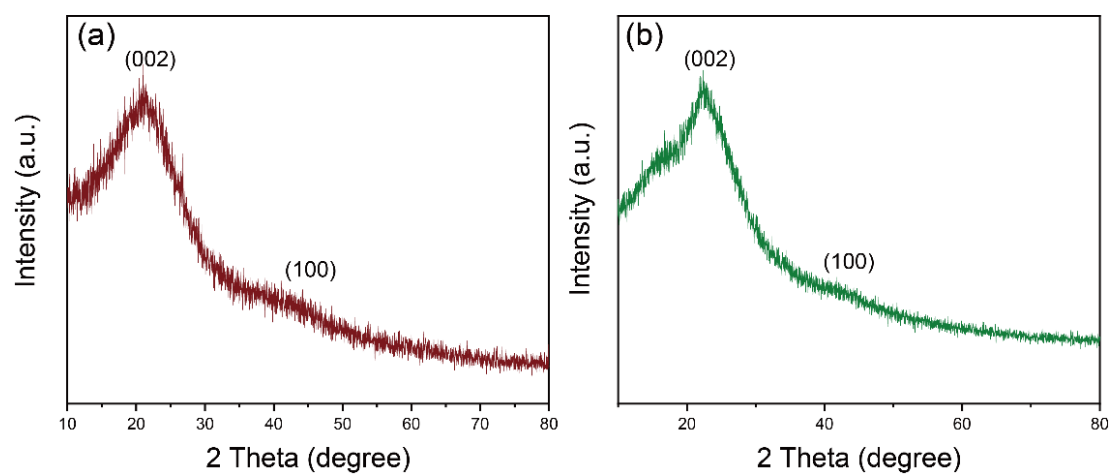**Figure S7** The removal efficiency of Cr(VI) and CTC over 5 cycles, related to **Figure 9**.

**Figure S8** XRD patterns of the NC synthesized from **(a)** cellulose and **(b)** corn cobs after reaction, related to **Figure 9 and Figure S7**.
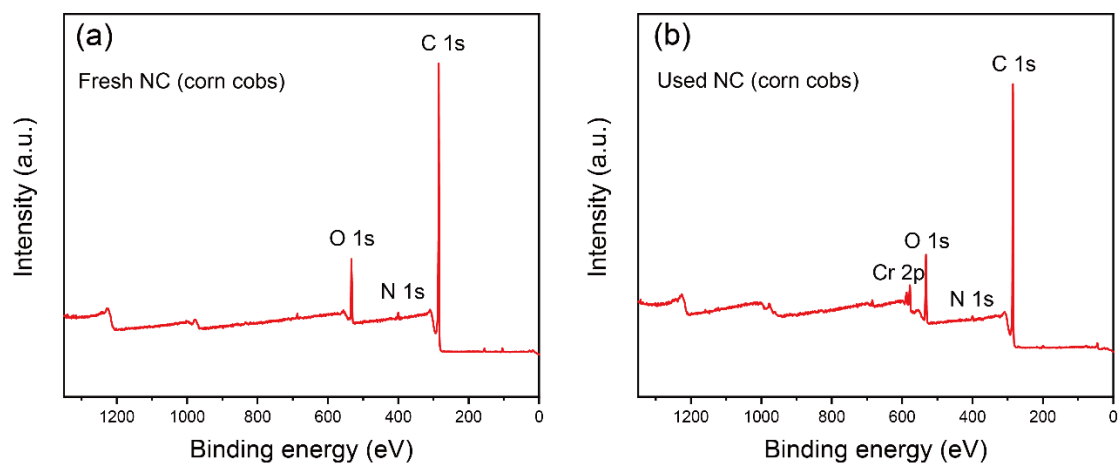
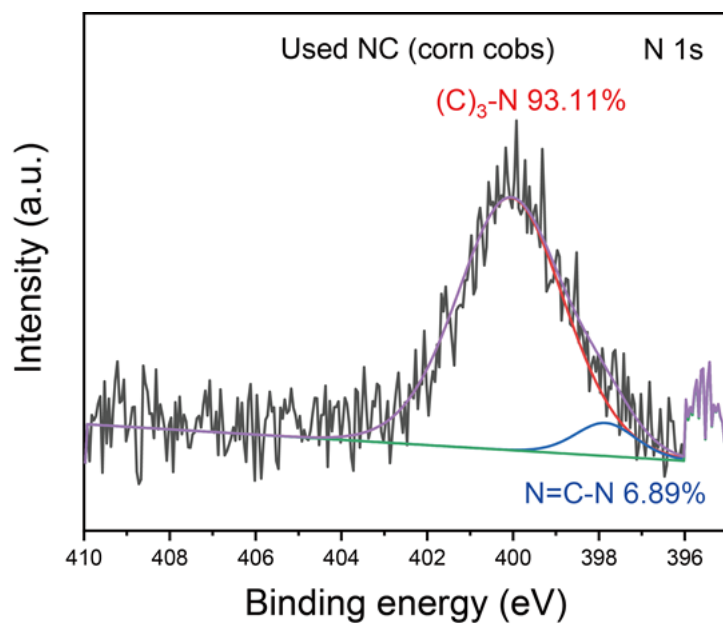**Figure S9** The full survey XPS spectra of **(a)** fresh and **(b)** used NC (corn cobs), related to **Figure 4, Figure S6, Figure S7 and Figure S8**.

**Figure S10** The high-resolution N 1s spectra of the used NC (corn cobs), related to **Figure 4, Figure S7 and Figure S8**.
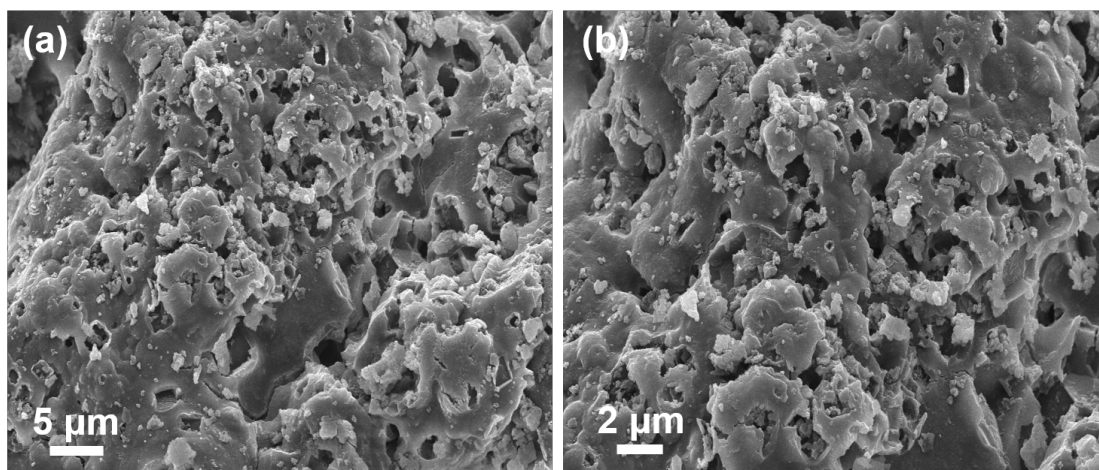
**Figure S11** SEM images of the used NC from corn cobs, related to **Figure 5, Figure S7, Figure S8 and Figure S10**.
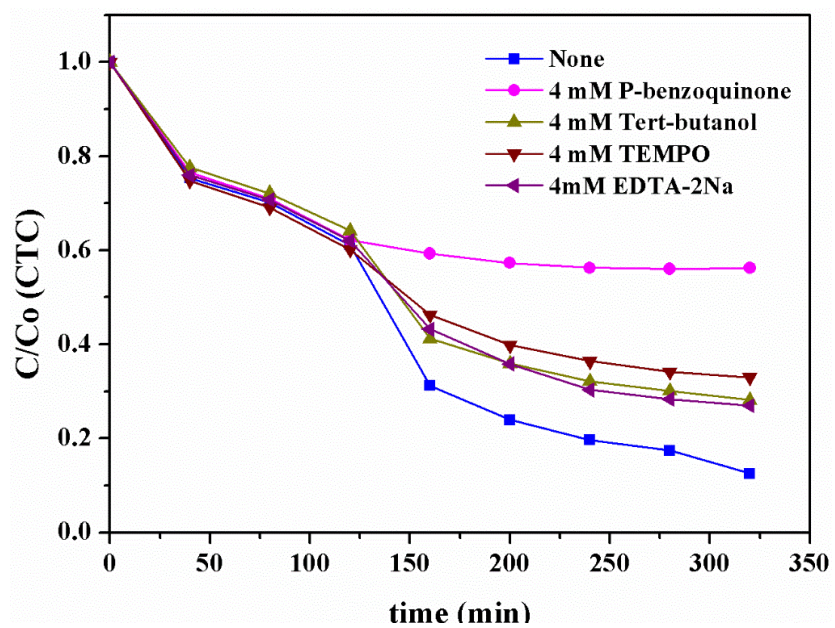
**Figure S12** Capture experiment of free radicals. Reaction conditions: Catalyst 0.1 g/L, CTC 6 mg/L, related to **Figure 11**.
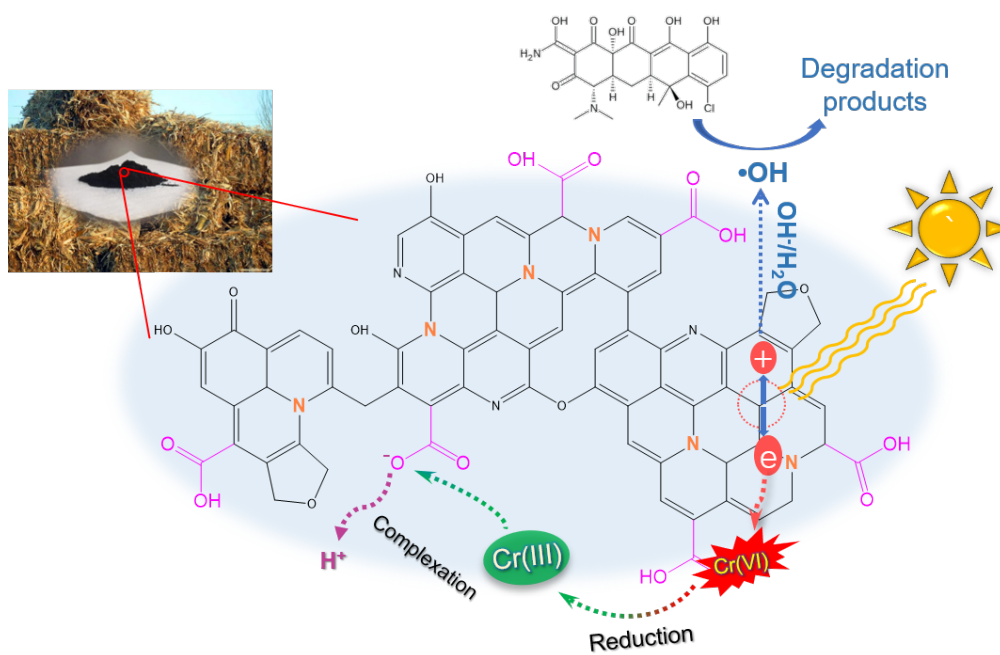
**Figure S13** Cooperation photocatalytic removal mechanism of Cr(VI) and CTC, related to **Figure 10**.